SP ISS: RECENT PROGRESS IN CHEMOMECHANICS

Microstructure Informed Mechanical Properties and Chemomechanical Degradation of Battery Cathode Particles

J. Han[1] · R. Ghosh[2] · F. Lin[2,3] · K. Zhao[1]

Abstract

Background Mechanical degradation of electrodes driven by electrochemical reactions limits battery performance and longevity. While various microstructures of $LiNi_xMn_yCo_zO_2$ (NMC) cathodes have been developed, their comparative mechanical properties and chemomechanical degradation are unknown.

Objective This study measures the mechanical properties of NMC cathode particles of three different microstructures: gravel-type NMC of large grains, gravel NMC of small grains, and rod-shaped NMC. Damage evolution in the NMC particles is simulated using finite element modeling.

Methods We use flat punch indentation to measure the particle strength, contact modulus, and fracture energy of NMC particles of different microstructures. We also assess the effect of voids on the mechanical properties and damage generation in NMC particles upon cycles.

Results The particle strength dictated by grain boundaries is measured to be ~ 200 MPa in the three NMC microstructures. The contact modulus changes nonlinearly during mechanical load. The fracture energy of gravel NMC particles is ~ 0.5 J/m^2. The presence of voids compromises the mechanical properties of NMC particles, but it helps delocalize stress within the particles and reduces damage generation upon electrochemical cycles.

Conclusions The combined experiments and modeling provide a comprehensive analysis of the mechanical behaviors and their implications on chemomechanical degradation of NMC cathode particles of various microstructures.

Keywords NMC cathode · Microstructure · Mechanical properties · Damage · Voids

Introduction

$LiNi_xMn_yCo_zO_2$ cathode of high Ni content is increasingly attractive for commercial Li-ion batteries due to the high capacity and low cost [1]. However, Ni-rich NMC suffers from rapid capacity fade during cycling, driven by both chemical and mechanical degradation [2–4]. Particle cracking in polycrystalline NMC is primarily induced by mismatched lattice deformation of neighboring primary particles during cycling. The anisotropic strains and stress concentration along grain boundaries promote intergranular fractures, leading to increased surface activities, electrical isolation, and rapid performance decay. Beyond particle cracking, other mechanical issues have drawn significant attention, especially in all-solid-state batteries [5], for example, the rigidness of solid-state electrolytes challenges their conformal contact with the electrodes, where contraction of active particles often causes loss of interfacial contact and particle expansion can crack the solid electrolyte. Mechanical degradation also occurs during electrode calendaring, an industrial process designed to densify electrode composites by applying an external pressure, which improves volumetric energy density, charge/discharge kinetics, and cycling stability [6, 7]. However, aggressive densification can crush active particles, leading to irreversible capacity loss even before cycling begins [8, 9]. These observations highlight the importance of understanding the mechanical behaviors of cathode particles to mitigate their degradation in battery manufacturing and operations.

✉ K. Zhao
  kjzhao@purdue.edu

1 School of Mechanical Engineering, Purdue University, West Lafayette, IN 47907, USA

2 Department of Chemistry, Virginia Tech, Blacksburg, VA 24061, USA

3 School of Engineering, Brown University, Providence, Rhode Island 02912, USA

The intrinsic mechanical properties of NMC materials, including elastic modulus, hardness, and toughness, have been widely studied as a function of the state of charge, cycle number, Ni content, and different electrolytes [10–13]. For example, the anisotropic stiffness matrix is obtained by correlating the measured local stiffness and lattice orientation [13]. Nevertheless, commercial composite cathodes are often made of NMC secondary particles – an aggregate form of primary particles of submicron size. The primary particles are held by Van der Waals forces. Therefore, the effective mechanical properties of NMC secondary particles can be largely different from the intrinsic material properties. For example, the mechanical strength of NMC secondary particles is determined by the grain boundaries between the primary particles rather than the intragranular strength. The commonly used sharp indentation tips, such as Berkovich and cube-corner tips, are difficult to be positioned at the grain boundaries to measure the interfacial properties. To determine the structural properties of polycrystalline NMC secondary particles, flat punch indentation has been used to evaluate the strength before the particles are crushed [14, 15]. Dang et al. found that the particle strength of $LiNi_{1/3}Mn_{1/3}Co_{1/3}O_2$ (NMC111) after the first lithiation and delithiation is significantly lower than the pristine values [16]. Whearcroft et al. evaluated the particle strength of $LiNi_{0.8}Mn_{0.1}Co_{0.1}O_2$ (NMC811) at different states of charge and observed dynamic crack propagation via *in situ* SEM imaging [17]. Shin et al. measured the breaking force of gradient core–shell NMC particles using nanoindentation, finding that particles with higher breaking forces exhibited improved capacity retention [18, 19]. A few other studies also attributed enhanced capacity retention to higher particle breaking forces [20, 21], however, without considering the effect of particle size. Since the size of NMC secondary particles can span from a couple of micrometers to tens of micrometers, the particle strength should be evaluated based on statistical sampling of different particle sizes. Furthermore, high particle strength alone does not necessarily predict better cycling performance. More studies on how the mechanical properties of electrodes regulate their electrochemical performance are needed.

Literature has reported many great efforts to mitigate cracking of NMC cathode. Strategies include doping, surface coating, single-crystalline design, and microstructure engineering [22]. Recent studies showed that rod-shaped/ultrafine primary particles, gradient/core–shell structures, and central porosity can help accommodate deformation and suppress crack propagation. NMC secondary particles of radially oriented primary particles mitigate cracking by favorable Li diffusion and reduced mismatch strain along grain boundaries [23–25]. The gradient or core–shell structured particles enable better mechanical stability at the surface and higher capacity density at the center [26]. Internal porosity also follows the same thought to accommodate the mechanical deformation [27–29]. In parallel, modeling has been used to study the effects of microstructure on Li diffusion kinetics, mechanical degradation, and electrochemical performance. Simulations show that rod-shaped NMC displays less damage than gravel-type particles due to more uniform deformation between neighboring grains [25, 30, 31]. The influence of grain size on mechanical degradation is not consistent in different studies. Some suggest that larger grains lead to less damage due to the lower density of grain boundaries, resulting in fewer sites of anisotropic mismatch chemical strains [32–35], whereas others argue that smaller grains are advantageous by distributing the strain field more evenly along the increased number of grain boundaries [30]. In contrast, some studies find minimal effects of grain size on mechanical degradation [36]. Overall, the microstructure of active particles plays an important role in modulating their mechanical behaviors, Li kinetics, damage dynamics, and capacity retention.

In this study, we measure the mechanical properties of Ni-rich NMC particles (NMC811) of three distinct microstructures: (1) gravel-type NMC secondary particles of large primary grains (900–1000 nm), (2) gravel-type NMC secondary particles of small grains (300–400 nm), and (3) rod-shaped NMC secondary particles of radially oriented primary grains. We will use Gravel_L, Gravel_S, and Rod to represent the three microstructures hereafter. The size of NMC secondary particles spans from a few micrometers to tens of micrometers. We use flat punch indentation to measure the particle strength, contact modulus, and fracture energy. We show that the particle strength of the three microstructures, predominated by the intergranular boundaries, is about 200 MPa. The particle strength is independent of the size of the secondary particles. Contact modulus of the particles changes nonlinearly at different compression depths. It is more of a structural response of the secondary particles that is different from the intrinsic elastic modulus of NMC materials. Fracture energy of gravel-type NMC is estimated to be about 0.5 J/m^2. To complement the experiments, we use finite element modeling (FEM) to understand the mechanical response of NMC secondary particles under flat punch indentation. The internal voids, populated at the intersections of grain boundaries, reduce the particle strength and elastic modulus. To bridge the relationship between the microstructure, mechanical properties, and electro-mechanical performance, we conduct cell modeling under multiple charging/discharging cycles. Interestingly, we find that the presence of voids helps delocalize stress in NMC polycrystalline particles and mitigate damage generation upon electrochemical cycles. Micro-voids might be an important element in NMC particles to help retain their structural integrity while experiencing anisotropic chemical strains during Li reactions.

Methods

Sample preparation: Gravel-type NMC811 of small grains is used as received from Rombei. To synthesize gravel NMC811 of large grains, as-received NMC811 is re-calcined at 800 °C for 6 h. For preparation of rod-shaped NMC811, a co-precipitated precursor is obtained from Shuangdeng Group Co., Ltd. The precursor is thoroughly ground with LiOH (dehydrated from LiOH·H2O, Sigma Aldrich. Purity 99.9%) using a mortar and pestle. The mixture is then calcined in two stages: first at 460 °C for 2 h, followed by a second calcination step at 750 °C for 6 h. An excess of 5 mol% LiOH is added to compensate Li loss during high-temperature calcination. Focused Ion Beam-Scanning Electron Microscopy (FIB-SEM) is performed using a Helios 5 Dual-Beam system to analyze both surface and cross-sectional morphologies of the NMC particles. Imaging is conducted at 5 kV and 0.10 nA.

Mechanical measurements: NMC811 cathode particles are dissolved and dispersed in IPA solvent inside an argon-filled glovebox with O_2 and H_2O content below 0.5 ppm. One drop of the solution is placed on an Al_2O_3 substrate, which is then dried for 10 min. Indentation test is performed using a Keysight G200 equipped with a 40-um flat punch tip, which is much larger than the particle size, ensuring that the flat tip boundary does not affect fracture of the particles. Continuous stiffness measurement (CSM) is used to measure the load and contact stiffness as a function of displacement. A harmonic displacement of 2 nm and a frequency of 45 Hz are set for CSM. The indenter is loaded at a constant strain rate at 0.05/s and stopped at a depth of 2000 nm. After each indentation, to remove potential residual particles attached to the tip, the indenter is pressed on an Aluminum sample to a depth of 4000 nm for 3 times. A 40X optical microscope is used to take images of pristine and crushed particles. ImageJ is used to calculate the particle diameter from the images of pristine particles.

We use Hiramatsu and Oka's model to determine the tensile strength of brittle, irregular particles [14]. The particle strength S_t is determined by

$$S_t \cong 2.8F_c/\pi d^2 \tag{1}$$

where F_c is the peak load and d is the particle diameter. Contact modulus E is obtained using Hertzian contact theory, which describes contact between flat surfaces with a spherical particle [37],

$$s = \frac{dF}{d\delta} = \left(6RE^{*2}F\right)^{\frac{1}{3}} \tag{2}$$

where s is the contact stiffness measured by CSM, F is the load, δ is the displacement, R is particle radius, and E^* is the reduced Young's modulus, which is a function of the mechanical properties of the particle and surfaces,

$$\frac{1}{E^*} = \frac{1 - v^2}{E} + \frac{1 - v_s^2}{E_s} \tag{3}$$

E (E_s) and v (v_s) are the modulus and Poisson's ratio of the particle (indenter tip or substrate). Since the particle is in contact with the tip on one end and with the substrate on the other, we calculate individual E at each contact and then do average to obtain the final value of particle contact modulus E. The dissimilarity in Young's modulus and Poisson's ratio of the indenter tip (diamond: 1140 GPa and 0.07) and the substrate (Al_2O_3: 380 GPa and 0.3) leads to a slight difference of displacement δ at each contact. For simplicity, we assume that the displacement is the same for both. Poisson's ratio of NMC is assumed to be 0.3. Since particle deformation under compression is relatively small ($< 10\%$), equation (2) is valid. We would like to emphasize that NMC particles are made of architectural polycrystalline grains, the contact modulus E here is different from the intrinsic stiffness of NMC materials.

When the particles are ruptured under compression, the fracture energy Γ is equal to the energy release rate G_c, defined as the decrease in elastic energy per unit area of fracture surface. In the crush experiments, we cannot monitor the intergranular crack growth, however, the energy release rate after the particle is crushed might be estimated by the applied energy U divided by the entire grain boundary area A,

$$\Gamma = \frac{U}{A} \tag{4}$$

where U is obtained by integrating the load–displacement curve until the particles are catastrophically crushed,

$$U = \int F d\delta \tag{5}$$

Given the brittle nature of NMC particles, we assume that the applied energy is stored as elastic energy in the deformed particles and fully released when the particles are pulverized. Furthermore, we assume that the load process is quasi-static under the strain rate of 0.05/s, and energy dissipation associated with particle deformation, possibly due to friction at the grain boundaries or wave propagation, is negligible. Under these assumptions, (equation (4)) provides an upper limit of fracture energy of NMC secondary particles upon complete rupture. To determine the fracture area A, 3D gravel-shaped particles with primary particle sizes of 400 nm and 800 nm, representing Gravel_S and Gravel_L, respectively, are modeled using the Voronoi function in MATLAB. The total surface area of the primary particles is used as an approximation of the fracture area.

Finite element modeling: We simulate flat punch indentation to model the stress distribution and crack propagation within secondary NMC particles under compression. In addition, we construct a half-cell of Li-ion batteries to simulate the voltage response, Li diffusion, stress evolution, and crack growth in NMC secondary particles during cycles. Primary particles of random shape in gravel-type NMC and their radial orientation in rod-shaped particles are generated by Voronoi tessellation in MATLAB. Micro-voids of various sizes are introduced at the intersections of primary particles as geometric defects. The void content is calculated by the ratio of the void area to the secondary particle area. We consider 2%, and 3.5% voids in gravel NMC particles.

The flat punch indentation model is constructed with a secondary NMC particle, a flat indent tip, and a substrate. The particle undergoes small deformation within the elastic region. The governing equations are as follows,

$$\varepsilon_{ij} = \frac{1}{2}\left(u_{i,j} + u_{j,i}\right) \tag{6}$$

$$\sigma_{ij} = \frac{E}{1+v}(\varepsilon_{ij} + \frac{v}{1-2v}\varepsilon_{kk}\delta_{ij}) \tag{7}$$

$$\sigma_{ij,j} = 0 \tag{8}$$

where ε_{ij} is the strain tensor, u_i is the displacement, and σ_{ij} is the stress tensor. E and v are elastic modulus and Poisson's ratio. We set the elastic modulus as 1141 GPa for the indent tip, 380 GPa for the substrate, and 200 GPa for NMC. Poisson's ratio is set as 0.07 for the indent tip and 0.3 for the substrate and particle. The penalty method is applied to simulate the contact between the indent tip and the particle, as well as the contact between the particle and the substrate,

$$T_n = \begin{cases} -p_n g_n, & g_n \le 0 \\ 0, & g_n > 0 \end{cases} \tag{9}$$

where T_n is the normal traction, p_n is the penalty factor, and g_n is the normal overlap displacement between the two contact surfaces. To simulate crack growth at the grain boundaries of primary particles, we use a cohesive zone model. Crack occurs in two steps: initiation and propagation. Before crack initiation, when the tractions t_n and t_s are less than the tensile and shear strength t_n^0 and t_s^0, the tractions t_n and t_s are proportional to the displacement d_n and d_s,

$$t_i = K_i d_i \tag{10}$$

where K_i is the stiffness for tensile and shear load. Once tractions exceed the threshold, damage initiates, and tractions decrease linearly. The area under the traction vs. displacement represents the critical energy release rate G_c. When the tractions between two contact surfaces become zero, damage is fully developed, and the damage parameter equals 1. For ease of convergence, we set the tensile strength t_n^0 as 200 MPa, t_s^0 as 100 MPa, critical energy release rate for tension as 2 J/m^2 and for shear as 1 J/m^2. A displacement boundary condition is applied to the top surface of the indenter tip. Applied force is recorded as the indenter moves downwards. A static simulation with a continuously increasing compression displacement is solved in COMSOL.

A half-cell model of Li-ion batteries is built to study the effect of particle microstructure on the electrochemical response and mechanical degradation during cycles. Electrochemistry of the model includes Li-ion diffusion in the electrolyte, electron conduction in the conductive matrix, interfacial charge transfer between the electrode and the electrolyte, and Li diffusion in the active particles. Mechanics of the cathode particle is simulated using the plane strain approximation. The total strain is composed of the chemical strain ε_{ij}^C and the elastic strain ε_{ij}^E,

$$\varepsilon_{ij} = \varepsilon_{ij}^E + \varepsilon_{ij}^C \tag{11}$$

$$\sigma_{ij} = C_{ijkl}\varepsilon_{kl}^E \tag{12}$$

Lithiation-induced chemical strain ε_{ij}^C is calculated from the change of the lattice parameters along the a- and c-axis during charging and discharging, and C_{ijkl} represents the anisotropic stiffness tensor. Cohesive zone model is applied along the grain boundaries. For simplicity, here we only consider crack opening as the major mechanism of intergranular damage and set the shear strength to be infinite. The simulation details of the governing equations, boundary conditions, and materials parameters can be found in our previous work [38]. We use the MUltifrontal Massively Parallel Sparse (MUMPS) direct solver in COMSOL to solve the co-evolution of Li concentration, stress, and damage in the half-cell model.

Results

Fig. 1 shows NMC secondary particles of different microstructures. SEM images of the overall particle morphology for gravel-type NMC of large grains, gravel-type NMC of small grains, and rod-shaped NMC are shown in Fig. 1(a), (d), and (g), respectively. The internal microstructures are viewed by cross-section FIB-SEM images in (b), (e), and (h). The gravel-type particles exhibit more randomly shaped grains with equal axes, whereas rod-shaped particles have radially oriented grains of extended radial length. Zoomed-in cross-section FIB-SEM imaging are shown in (c), (f), and (i). The primary particle size is about 900–1000 nm for large-grain gravel particles and 300–400 nm for small-grain
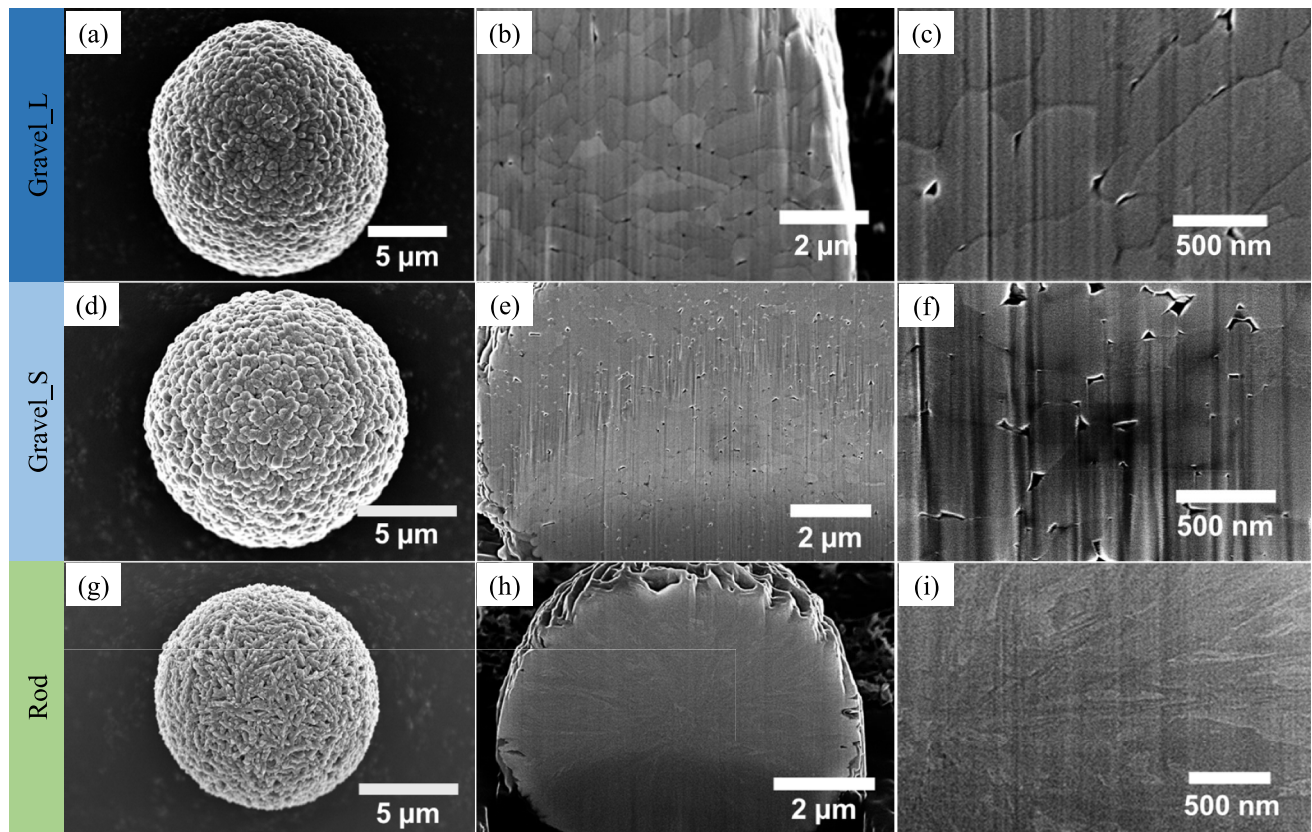
Fig. 1 SEM images showing the microstructures of (**a-c**) gravel-type NMC secondary particles of large primary particles (900–1000 nm), (**d-f**) gravel-type NMC secondary particles of small primary particles (300–400 nm), and (**g-i**) rod-shaped NMC secondary particles. Micro-voids are populated at the intersections of grain boundaries of gravel NMC

ones. Rod-shaped particles have needle-like grains with a radial length of around 500 nm and a much smaller width. Additionally, voids are present at the intersections of neighboring primary particles in the gravel particles, with an estimate of 2% in large-grain gravel particles and 4% in small-grain gravel particles from the SEM images. In contrast, rod-shaped particles do not show any internal voids. The presence of internal voids, along with the grain shape and size, plays an important role in the mechanical properties and electrochemical degradation of NMC secondary particles.

The load–displacement curves in flat punch indentation tests are shown in Fig. 2 (a)-(c) for large-grain gravel, small-grain gravel, and rod-shaped NMC particles, respectively. As the indenter tip compresses the particles, load increases nonlinearly until it reaches the peak value which indicates that particles are crushed. The peak load is used to calculate the particle strength. The dashed lines are drawn to show the point of catastrophic failure of the particles, where the force sensor is unable to record the load. The color of each curve represents the size of NMC secondary particles measured for each microstructure. Clearly, larger particles are crushed at higher peak loads. We choose to indent particles of diameter

ranging from 4 to 16 um to examine the effect of secondary particle size. The built-in 40X optical microscope captures images of the pristine and crushed particles for different particle sizes, Fig. 2(d). All particles are crushed into flattened shapes, where fracture occurs along most of the grain boundaries. While most of the particles after the test remain on the substrate, some small pieces might be stuck to the tip, such as the 4 um particles. ImageJ is used to determine the particle diameter from images of pristine particles.

Fig. 3 summarizes the peak load and particle strength of NMC secondary particles of three different microstructures. The relationship between the peak load and the diameter of NMC particles is shown in Fig. 3 (a)-(c) for gravel NMC of large grains, gravel NMC of small grains, and rod-shaped NMC, respectively. The inset schematics, made by Blender, illustrate the microstructures of these three types of particles. The peak load is in the range of 1–60 mN and increases monotonically with the particle size. Equation (1)is used to calculate the particle strength. The measured strengths are around 200 MPa, which is consistent with literature results [16]. Particle strength represents the bonding strength between the constituent primary grains and is considered as a structural property of NMC secondary particles synthesized at specific
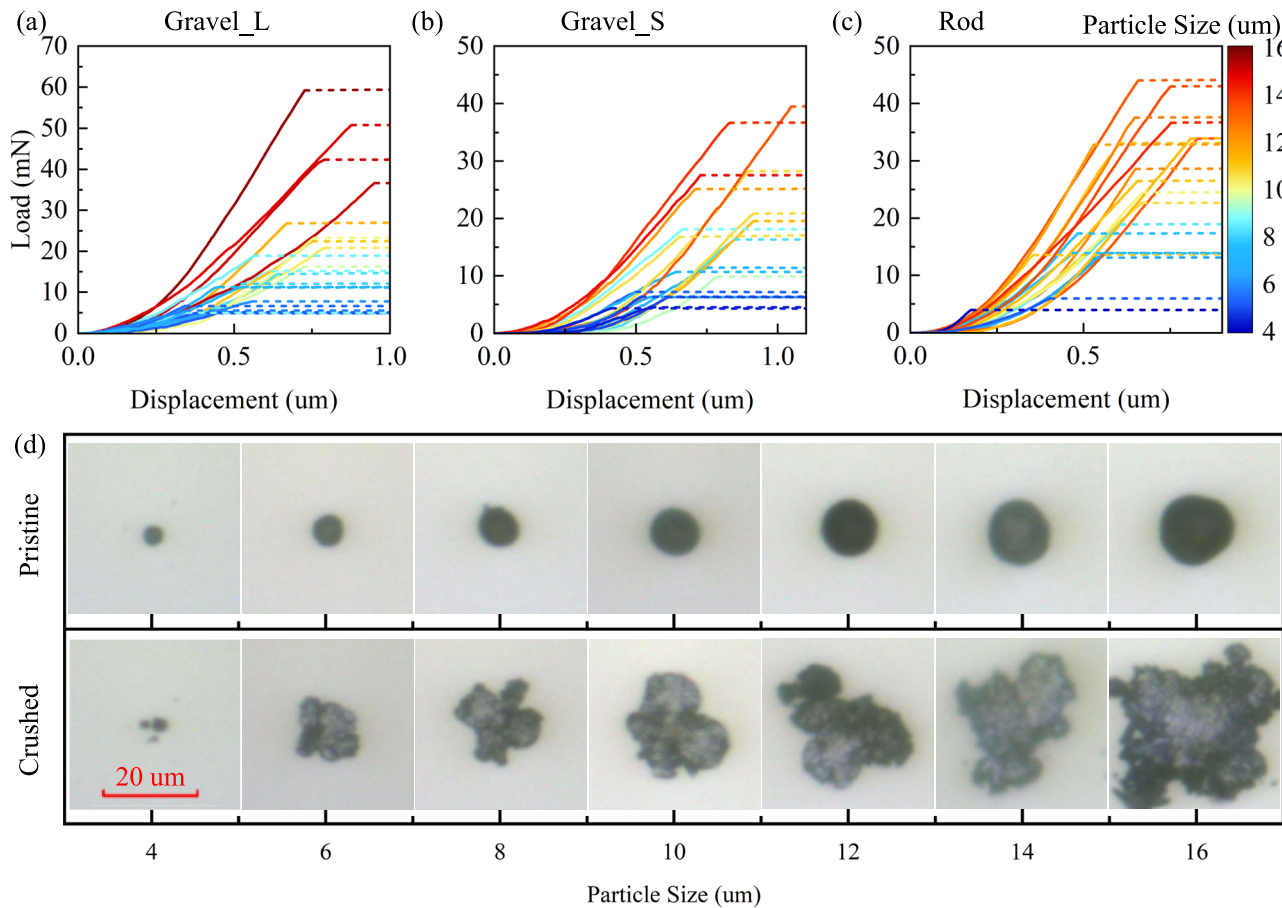
Fig. 2 Load–displacement curves of flat punch indentation on (**a**) gravel NMC of large grains, (**b**) gravel NMC of small grains, and (**c**) rod-shaped NMC. The color scheme represents the size of secondary particles. (**d**) Optical images showing the morphology of pristine and crushed NMC particles where the diameter of secondary particles varies from 4 to 16 um

conditions. Here, the three types of NMC particles are made of anisotropic primary grains with varying shapes and sizes. The microstructure might change the stress distribution and magnitude, which in turn affects the maximum force a particle can withstand. Despite this, the experimental results show that there is limited variation in particle strength among the three microstructures as summarized in Fig. 3(d)-(f), where the mean strength for large-grain gravel NMC is 172.8 MPa, small-grain gravel NMC is 180 MPa, and rod-shaped NMC is 210.6 MPa. The secondary particle size for a given microstructure has no effect on the particle strength. The small-grain gravel NMC has slightly higher strength than the large-grain ones. The rod-shaped NMC shows better strength than gravel-type particles. A recent study [39] showed that rod-shaped NMC particles have substantially increased percentage of low-angle grain boundaries and twin boundaries which contribute to the enhanced cohesion strength of the primary grains. Another contributing factor might be the micro-voids presented at the junctions of intergranular boundaries of gravel NMC particles, which concentrate stress and reduce the

particle strength. In the following, we will use computational modeling to further study the effect of voids.

Fig. 4 plots contact modulus of NMC secondary particles which is calculated from the continuous stiffness measurement in (equations (2) and (3)). We highlight that contact modulus is different from the intrinsic stiffness of NMC materials because secondary particles are an agglomerated form of primary grains which are subject to sliding along the grain boundaries and densification upon compression. Contact modulus is an important structural parameter to evaluate the local stress in NMC cathode during calendaring process. Fig. 4(a)-(c) show the contact modulus at different compression strains until the particles are crushed for large-grain gravel NMC, small-grain gravel NMC, and rod-shaped NMC particles, respectively. The engineering strain is calculated by the compression displacement divided by the particle diameter. For each microstructure, the average value within a given range of secondary particle size (solid lines) and the standard deviation (shaded regions) are plotted. The gradient colors of the solid lines represent the particle size. The overlap
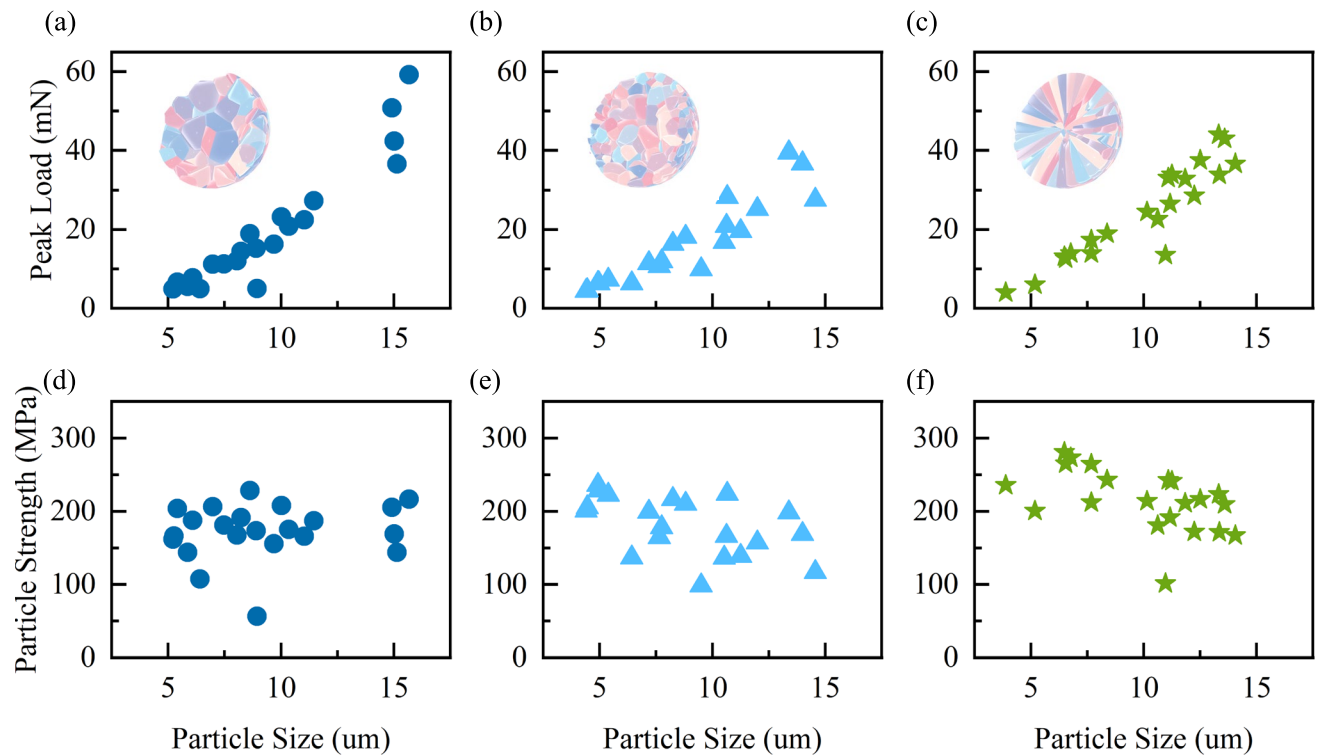
Fig. 3 Peak load as a function of the secondary particle size for (**a**) gravel NMC of large grains, (**b**)gravel NMC of small grains, and (**c**) rod-shaped NMC. The inset images are schematics of each microstructure. (**d-f**) show the particle strength of the three NMC of different secondary particle sizes
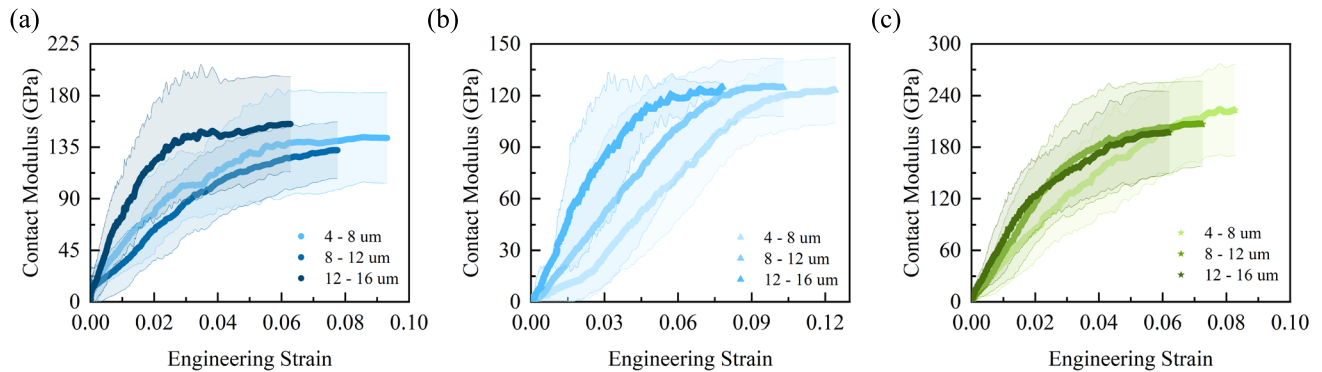

Fig. 4 Contact modulus of (**a**) gravel NMC of large grains, (**b**) gravel NMC of small grains, and (**c**) rod-shaped NMC at different compression displacements. The gradient colors represent different ranges of secondary particle size and the shaded areas are the standard deviation

of the three sets of sample sizes indicates that the contact modulus has a weak correlation with the secondary particle size. The contact modulus increases with the indentation displacement and eventually converges to a plateau before the particles are crushed. The initial small value in contact modulus is likely due to particle surface roughness. The nonlinear contact modulus of NMC secondary particles is interesting and never reported in literature. It can be used to evaluate the internal stress in composite electrodes due to contact between

the active particles and their surrounding matrix. The chemical strain in NMC upon charging and discharging is < 5%, and within this deformation, NMC particles are quite compliant compared to the intrinsic elastic modulus of NMC materials. This indicates that the stress at the interface between NMC particles and the conductive matrix is small during cycles. Among the three microstructures, the rod-shaped NMC exhibits the highest contact modulus due to the increased grain strength brough by the low-angle and twin boundaries, which

resist sliding between the primary grains. It is also noteworthy that, for a given microstructure, the smallest secondary particles sustain the largest fracture strain. This is likely because the small secondary particles contain less grain boundaries, which contribute to the failure strain. Nevertheless, the plateau values of contact modulus for different sets of samples sizes are about the same for each microstructure.

Fig. 5 summarizes the measured mechanical properties of NMC particles of different microstructures. Fig. 5(a) is a replot of the particle strength collecting all particle sizes for each microstructure. Fig. 5(b) shows the particle modulus, defined as the plateau value of contact modulus of NMC secondary particles under compression. The mean values of particle modulus are 139 GPa for large-grain gravel NMC, 122 GPa for small-grain gravel NMC, and 204 GPa for rod-shaped NMC. Two reference dashed lines in Fig. 5(b) represent elastic modulus of sintered NMC pellets (200 GPa) and agglomerated particles (113 GPa) measured using a Berkovich tip [11]. Particle modulus of gravel NMC aligns with that of agglomerated particles, while the value of rod-shaped NMC is close to that of sintered pellets, indicating different characteristics of grain boundaries. The similarity between gravel NMC and agglomerated particles is expected, as they represent the same type of samples. Sintered pellets are composed of 3–10 μm large primary grains, therefore, their elastic modulus approximates the intrinsic properties of NMC materials. The property of rod-shaped NMC is also close to the intrinsic value due to its grain alignment, strong cohesion strength of primary grains, and low porosity. For gravel NMC of different primary particle sizes, large-grain ones contain less grain boundaries and are more resistant to sliding, leading to a higher particle modulus. Sintered pellets follow this trend, and single-crystalline particles would be the extreme case. Micro-voids undermine the elastic properties as described by the rule of mixture, in NMC secondary particles, they further concentrate stresses and initiate damage at the intersection of grain boundaries which reduce the particle modulus. Fig. 5(c) shows the fracture energy of gravel-type NMC calculated by equations (4) and (5), which is around 0.5 J/m^2. More specifically, the average fracture

energy for large-grain gravel NMC particles is 0.69 J/m^2, and for small-grain particles, it is 0.46 J/m^2. It is noted that the average fracture energy of secondary particles of large primary grains is higher than that of small-grain ones. The reason behind this difference is unclear at this writing. Nevertheless, these values are found to be consistent with our previously reported values measured using a Berkovich tip [13]. Fracture energy of rod-shaped NMC is not calculated because of the irregular shape of primary grains, and surface area of grain boundaries cannot be determined.

To understand the mechanical behavior of NMC particles, especially its dependence on the presence of micro-voids, we conduct finite element modeling to simulate flat punch indentation on continuous particles and gravel-type NMC particles. Since we do not observe any major differences in mechanical behaviors of gravel NMC of large and small primary grains in experiments, here we only simulate one given size of primary grains in NMC particles. Fig. 6(a)-(b) show the profiles of shear stress τ_{xy} and tensile stress σ_x within a continuous particle at a given indentation displacement. The maximum shear stress occurs at the top and bottom of the particle between the contact with the tip, while the maximum tensile stress is presented along the vertical diametrical direction (*y*-axis). The upper and lower limits of the color bar are manually set to include the major values of stresses within the particle while avoiding numerical singularities at the contact. The simulation results are consistent with the analytical solution of indirect tension tests [40], which validates the numerical modeling. To compare the load capacity of NMC secondary particles at different void contents, Fig. 6(c) shows the load vs. displacement responses under flat punch compression of gravel-type NMC without voids, and gravel NMC with 2% and 3.5% voids populated at the intersections of primary grains. A linear compression displacement is applied until the particle is completely crushed and unable to withstand any force. Micro-voids significantly reduce the peak load that NMC particles can sustain, because voids concentrate stress and compromise the particle strength. Particle modulus follows the same trend due to the facilitated grain sliding by voids. Here, particle contact
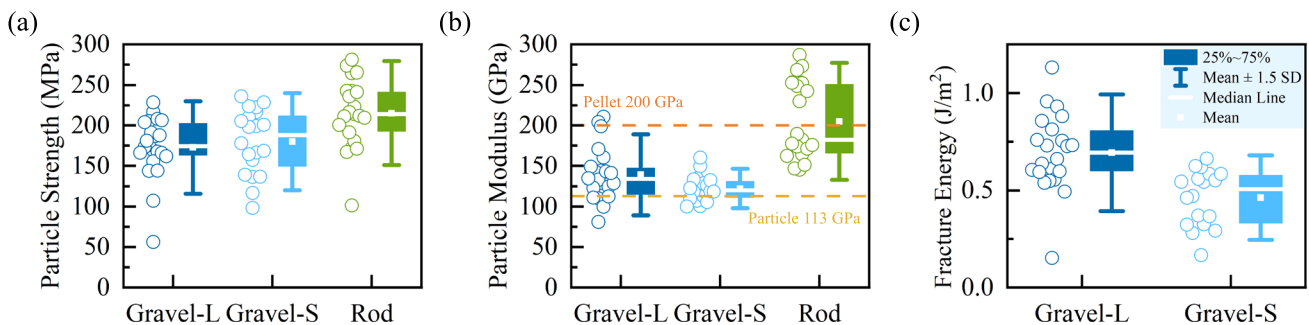

Fig. 5 (a) Particle strength, (b) particle modulus, and (c) fracture energy for NMC particles of different microstructures. The dashed lines in (b) mark the elastic modulus of NMC sintered pellets and agglomerated particles measured using a Berkovich tip [11]
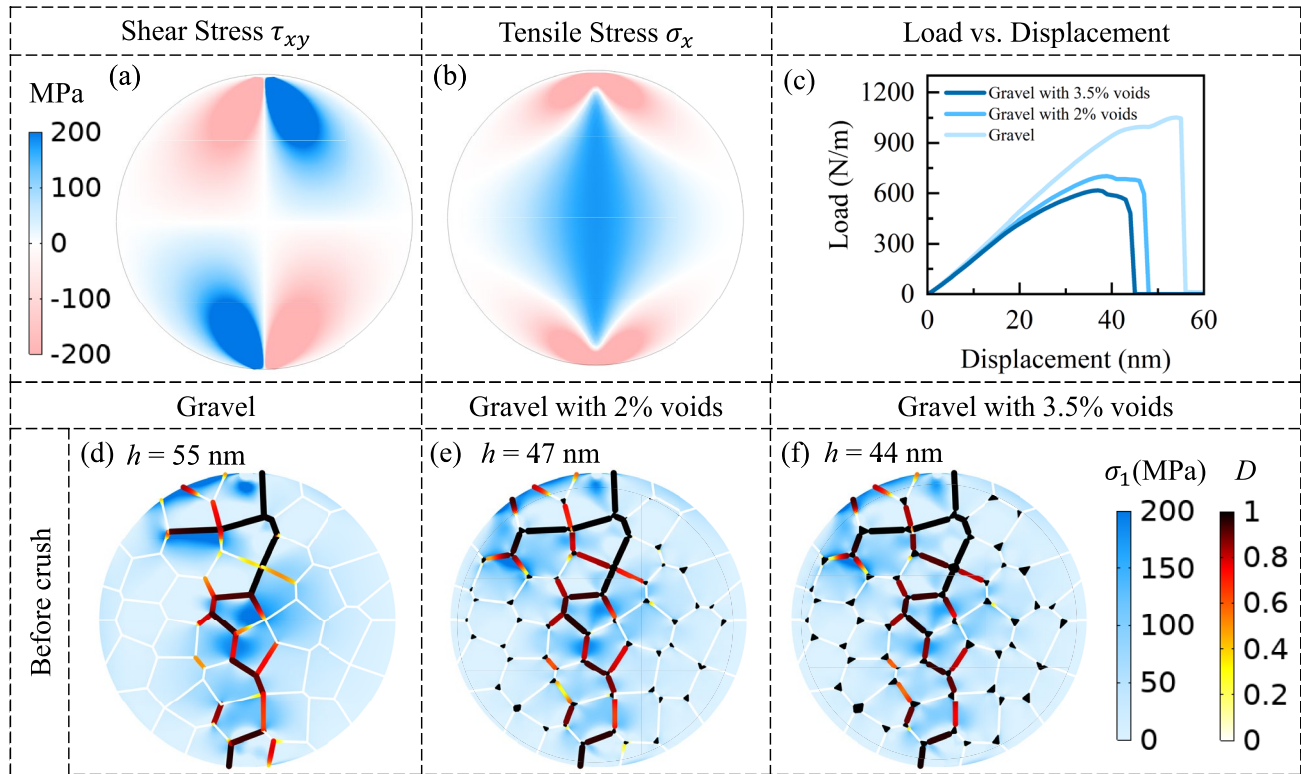
Fig. 6 FEM modeling of mechanical behaviors of NMC particles upon flat punch indentation. (**a**) Shear stress and (**b**) tensile stress profiles for a continuous particle at the indentation displacement $\delta = 80$ nm. (**c**) Load–displacement curves for gravel-type NMC without voids, and gravel NMC with 2% and 3.5% voids populated at the intersections of primary grains. (**d-f**) show the distributions of the first-principal stress and damage before the secondary particles are crushed. The presence of micro-voids reduces both particle strength and particle modulus

modulus is determined by least-square fitting the load–displacement curve with the analytical solution for 2D contact between a rigid plane and a deformable cylinder [41]:

$$\delta = \frac{F}{\pi L E^*}\left[1 + \ln\left(\frac{2\pi L^3 E^*}{FD}\right)\right] \quad (13)$$

where δ is the displacement, F is the load, E^* is the reduced elastic modulus as shown in equation (3), D is the diameter of the sphere, and L is the thickness in the out-of-plane direction which we assume to be the particle diameter. With 2% and 3.5% voids, particle modulus decreases by 7% and 12%, respectively, largely deviating from the rule of mixture. Fig. 6(d-f) show the distributions of the first-principal stress and damage along the grain boundaries in the three gravel NMC secondary particles. Damage initiates from the top and bottom surfaces of the particles upon application of flat punch due to the developed shear stress exceeding the shear strength of grain boundaries. Before the particles are catastrophically crushed, major cracks are formed along the vertical diametric direction, primarily driven by the tensile stress developed along the y-axis. The stress profiles also explain the similar behavior of gravel NMC particles of large and small primary grains. When the grain boundaries are aligned with the direction of the maximum shear

stress, mechanical damage is more likely to initiate. Likewise, when the primary grains are located along the y-axis where the maximum tensile stress takes place, intergranular cracks are more prone to occur. Therefore, the grain size or shape does not largely influence the particle strength. Nevertheless, the presence of micro-voids increases the compliance of NMC particles and facilitates crack initiation and propagation as shown in the comparison between the NMC particles without and with voids in Fig. 6(d)-(f). Voids at the intersections of grain boundaries concentrate stress and lead to earlier particle fracture under mechanical load.

To bridge the mechanical properties of NMC particles and their electrochemical performance, we conduct electro-chemo-mechanical modeling in a half-cell setting comprised of NMC cathode and Li anode. Details of the electrochemistry modeling are described in the Methods section. Here, we focus on the implication of the grain size and presence of micro-voids on development of intergranular damage in NMC secondary particles. The cell is charged at 1 C rate with a voltage window of 3.55–4.25 V. Fig. 7(a)-(d) show Li concentration profiles at the end of the first charging for gravel-type NMC of large grains, gravel NMC of small grains, and small grains with 2% and 3.5% voids, respectively. We should note that the modeling adopts isotropic diffusion without differentiating Li diffusivities in the

ab plane versus along the *c*-axis of NMC. This 2D isotropic diffusion model replicates the core–shell Li concentration profile along the radial direction in a 3D secondary particle with anisotropic diffusivities assigned in the *ab* plane and along the *c*-axis. The 2D model largely reduces the computational cost while enabling simulations of damage network in the intergranular structure. To capture the mechanical behaviors of NMC particles, we have included the anisotropic mechanical properties and anisotropic chemical strains of NMC upon charging. The concentration profiles in Fig. 7(a)-(d) are similar given the nature of isotropic diffusion. However, intergranular damage is largely dependent on the microstructure. In Fig. 7(e)-(h), the blue gradient color shows the first-principal stress within the particles and the black lines represent the cohesive fracture. The intergranular damage shows a random distribution in gravel-type particles of both large and small grains because of anisotropic mismatch strains of the primary grains. The mismatch strains concentrate stress at the intersections of the grain boundaries where mechanical damage is mostly initiated from. We should note that the observations in different grain sizes remain qualitative. The grain sizes in experiments are 300–400 nm for small-grain gravel particles and 900–1000 nm for large-grain ones, the modeling cannot preciously match these sizes due to the computational limitation when damage is incorporated. In addition,

we have not considered electrolyte penetration along the cracked grain boundaries and its corrosion effect on the mechanical strength which were considered in our previous study [38]. The grain size effect on intergranular fracture remains an open question for future experiments and modeling. An interesting finding is the void effect, which is demonstrated in Fig. 7(g) and (h). NMC particles with internal voids show lower values of the first-principal stresses, as shown by the gradient blue color, and reduced mechanical damage. Voids delocalize stresses and prevent excessive cracking by accommodating anisotropic strains along the grain boundaries. In aggregated NMC secondary particles, stress is primarily generated by mismatch strains between neighboring, disoriented anisotropic grains, especially at the junctions where multiple grains meet. The presence of micro-voids deconcentrates stresses and mitigates damage initiation at those weak spots. Interestingly, micro-voids present contrasting effects in the mechanical properties of NMC particles under mechanical load and chemo-mechanical degradation in cycles. In the flat punch experiments, voids compromise particle strength due to stress concentration and reduce particle modulus due to grain sliding. In contrast, voids benefit the structural integrity of NMC cathode particles upon charging because of delocalization of stresses induced by anisotropic chemical strains.
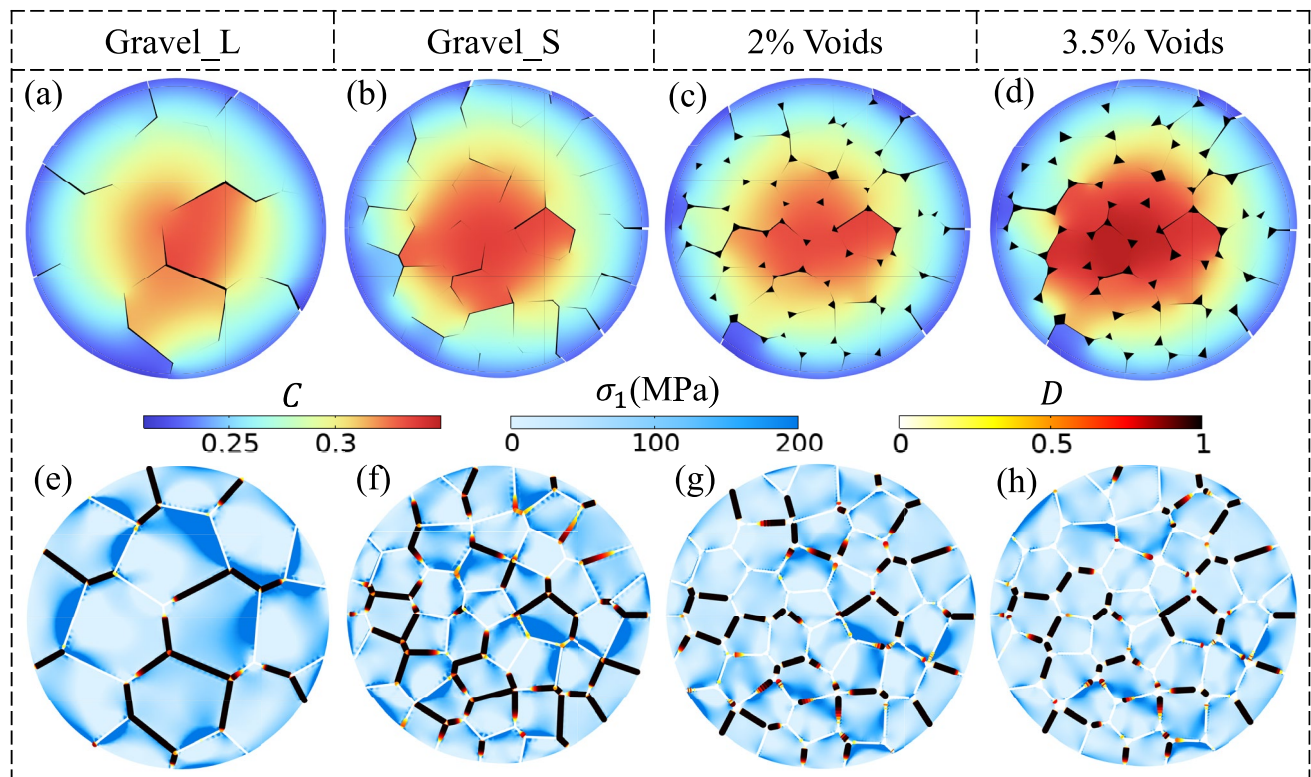

Fig. 7 The upper figures (**a**)-(**d**) show Li concentration distributions at the end of the first charging in gravel NMC of large grains, gravel NMC of small grains, and small grains with 2% and 3.5% voids, respectively. The lower figures (**e**)-(**h**) show the corresponding first-principal stress and damage profiles. The presence of voids delocalizes stress and reduces mechanical damage upon charging
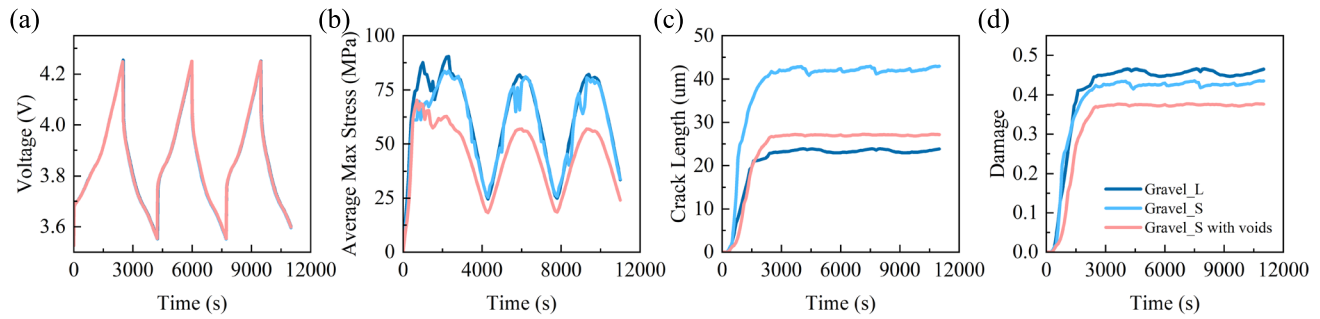
Fig. 8 (**a**) Voltage responses, (**b**) average first-principal stress within NMC secondary particles, (**c**) crack length, and (**d**) damage evolution of gravel-type NMC of large grains, small grains, and small grains of 3.5% voids over the first three cycles

Fig. 8 shows the quantitative comparison of the electro-chemical response and damage evolution of gravel-type NMC particles of large grains, small grains without voids, and small grains with 3.5% voids at the intersections of grain boundaries in the first three charging-discharging cycles. The results for 2% and 3.5% voids are nearly the same, which indicates the size independence of voids on damage mitigation which is discussed in Fig. 7. The impact of the grain size, micro-voids, and intergranular damage on Li kinetics is minimal as evidenced by the overlapping voltage curves shown in Fig. 8(a). This is expected because the voltage response is primarily determined by the surface charge transfer kinetics – it is the same when the secondary particle size is fixed at a given charging rate. When electrolyte penetration is considered along the freshly cracked surfaces, cell capacity would be enhanced due to the enlarged surface area and facilitated Li diffusion along the damage net-work [38]. Fig. 8(b) shows the average first-principal stress within the secondary particles over cycles which indicate tensile cracking along the grain boundaries. The stress profile follows the same oscillating pattern of the charging-discharging curves due to the breathing chemical strains in NMC lattice associated with Li reactions. The first-principal stress reaches a peak value at the end of the first charging, and its peak values in subsequent cycles slightly decrease due to cracking. The stress profiles are about the same for NMC particles of large and small grains which is again due to the similar mismatch strain field of the constituent primary grains. However, the first-principal stress in NMC particles of internal voids is largely reduced because of stress deconcentration. Fig. 8(c) shows the overall crack length in the three particles. The small-grain particle without voids has the longest crack length because of more grain boundaries compared to the large-grain sample. Crack length should be discussed in the context of grain size to represent the structural damage of cathode particles. NMC particles with micro-voids have a much-reduced crack length compared to the void-free counterpart due to the stress release. Damage evolution upon cycles in the three NMC particles is shown in Fig. 8(d). The comparison is consistent with what has been discussed earlier. It is interesting to note that intergranular damage is saturated at

the end of the first charging because of the oscillating internal stresses and no further growth of elastic energy in NMC particles in subsequent cycles. This might be an oversimplified picture given the complex coupling of degradation in batteries and fatigue growth over cycles. Nevertheless, it indicates that significant mechanical damage is developed in early cycles of cathode particles of the characteristic intergranular structure.

Conclusions

We study the mechanical properties and chemomechanical damage of NMC cathode particles of different microstructures using small-scale experiments and computational modeling. Rod-shaped NMC secondary particles and gravel-type NMC of large and small grains are synthesized. We use flat punch indentation experiments to measure the particle strength, contact modulus, and fracture energy of single NMC particles with a large range of particle sizes. While the mechanical properties of gravel NMC remain close, rod-shaped NMC outperforms in particle strength and modulus given its higher cohesion strength of grain boundaries and absence of voids. The experiments provide useful information to compare the mechanical strength of cathode particles of different microstructures and can be used to evaluate damage development in single cathode particles as well as internal stress in composite electrodes due to mechanical contact. We perform computational modeling of NMC particles under mechanical load and upon electrochemical cycles to gain mechanistic under-standing. Under flat punch compression, micro-voids popu-lated at the intersections of grain boundaries compromise the particle strength due to stress concentration and reduce the particle modulus due to grain sliding. However, voids benefit the structural integrity of NMC secondary particles over cycles by delocalizing stresses induced by anisotropic chemical strains and preventing excessive cracking in the intergranular structure.

Declarations

References

1. Manthiram A (2020) A reflection on lithium-ion battery cathode chemistry. Nat Commun 11:1550. https://doi.org/10.1038/s41467-020-15355-0
2. Britala L, Marinaro M, Kucinskis G (2023) A review of the degradation mechanisms of NCM cathodes and corresponding mitigation strategies. J Energy Storage 73:108875. https://doi.org/10.1016/j.est.2023.108875
3. Jiang M, Danilov DL, Eichel RA, Notten PHL (2021) A review of degradation mechanisms and recent achievements for Ni-rich cathode-based Li-ion batteries. Adv Energy Mater 11:2103005. https://doi.org/10.1002/aenm.202103005
4. Li T, Yuan XZ, Zhang L et al (2020) Degradation mechanisms and mitigation strategies of nickel-rich NMC-based lithium-ion batteries. Electrochem Energ Rev 3:43–80. https://doi.org/10.1007/s41918-019-00053-3
5. De Vasconcelos LS, Xu R, Xu Z et al (2022) Chemomechanics of rechargeable batteries: status, theories, and perspectives. Chem Rev 122:13043–13107. https://doi.org/10.1021/acs.chemrev.2c00002
6. Tao R, Steinhoff B, Uzun K et al (2023) Correlation among porosity, mechanical properties, morphology, electronic conductivity and electrochemical kinetics of dry-processed electrodes. J Power Sources 581:233481. https://doi.org/10.1016/j.jpowsour.2023.233481
7. Abdollahifar M, Cavers H, Scheffler S et al (2023) Insights into influencing electrode calendering on the battery performance. Adv Energy Mater 13:202300973. https://doi.org/10.1002/aenm.202300973
8. Heenan TMM, Wade A, Tan C et al (2020) Identifying the origins of microstructural defects such as cracking within Ni-rich NMC811 cathode particles for lithium-ion batteries. Adv Energy Mater 10:2002655. https://doi.org/10.1002/aenm.202002655
9. Huttner F, Diener A, Heckmann T et al (2021) Increased moisture uptake of NCM622 cathodes after calendering due to particle breakage. J Electrochem Soc 168:090539. https://doi.org/10.1149/1945-7111/ac24bb
10. Xu R, Sun H, Scalco De Vasconcelos L, Zhao K (2017) Mechanical and structural degradation of LiNi x Mn y Co z O 2 cathode in Li-ion batteries: an experimental study. J Electrochem Soc 164:3333–3341. https://doi.org/10.1149/2.1751713jes
11. De Vasconcelos LS, Sharma N, Xu R, Zhao K (2019) In-situ nanoindentation measurement of local mechanical behavior of a Li-ion battery cathode in liquid electrolyte. Exp Mech 59:337–347. https://doi.org/10.1007/s11340-018-00451-6
12. Cheng EJ, Hong K, Taylor NJ et al (2017) Mechanical and physical properties of LiNi0.33Mn0.33Co0.33O2 (NMC). J Eur Ceram Soc 37:3213–3217. https://doi.org/10.1016/j.jeurceramsoc.2017.03.048
13. Sharma N, Meng D, Wu X et al (2023) Nanoindentation measurements of anisotropic mechanical properties of single crystalline NMC cathodes for Li-ion batteries. Extrem Mech Lett 58:101920. https://doi.org/10.1016/j.eml.2022.101920
14. Hiramatsu Y, Oka Y (1966) Determination of the tensile strength of rock. Int J Rock Mech Min Sci 3:89–99. https://doi.org/10.1016/0148-9062(66)90002-7
15. Yoshida M, Ogiso H, Nakano S, Akedo J (2005) Compression test system for a single submicrometer particle. Rev Sci Instrum 76:093905. https://doi.org/10.1063/1.2038187
16. Dang D, Wang Y, Cheng Y-T (2019) Communication—Fracture behavior of single LiNi 0.33 Mn 0.33 Co 0.33 O 2 particles studied by flat punch indentation. J Electrochem Soc 166:A2749–A2751. https://doi.org/10.1149/2.0331913jes
17. Wheatcroft L, Bird A, Stallard JC et al (2023) Fracture testing of lithium-ion battery cathode secondary particles *in-situ* inside the scanning electron microscope. Batteries Supercaps 6:e202300032. https://doi.org/10.1002/batt.202300032
18. Shin Y, Maeng S, Chung Y et al (2021) Core–multishell-structured digital-gradient cathode materials with enhanced mechanical and electrochemical durability. Small 17:202100040. https://doi.org/10.1002/smll.202100040
19. Maeng S, Chung Y, Min S, Shin Y (2020) Enhanced mechanical strength and electrochemical performance of core–shell structured high–nickel cathode material. J Power Sources 448:227395. https://doi.org/10.1016/j.jpowsour.2019.227395
20. Ju P, Ben L, Li Y et al (2023) Designer particle morphology to eliminate local strain accumulation in high-nickel layered cathode materials. ACS Energy Lett 8:3800–3810. https://doi.org/10.1021/acsenergylett.3c01272
21. Park GT, Yoon DR, Kim UH et al (2021) Ultrafine-grained Ni-rich layered cathode for advanced Li-ion batteries. Energy Environ Sci 14:6616–6626. https://doi.org/10.1039/d1ee02898g
22. Zhang Y, Kim JC, Song HW, Lee S (2023) Recent achievements toward the development of Ni-based layered oxide cathodes for fast-charging Li-ion batteries. Nanoscale 15:4195–4218. https://doi.org/10.1039/d2nr05701h
23. Wang Z, Wei W, Han Q et al (2023) Isotropic microstrain relaxation in Ni-rich cathodes for long cycling lithium ion batteries. ACS Nano 17:17095–17104. https://doi.org/10.1021/acsnano.3c04773
24. Park GT, Park NY, Ryu HH et al (2024) Nano-rods in Ni-rich layered cathodes for practical batteries. Chem Soc Rev 53:11462. https://doi.org/10.1039/d3cs01110k
25. Xu Z, Jiang Z, Kuai C et al (2020) Charge distribution guided by grain crystallographic orientations in polycrystalline battery materials. Nat Commun 11:1–9. https://doi.org/10.1038/s41467-019-13884-x

26. Sun YK, Chen Z, Noh HJ et al (2012) Nanostructured high-energy cathode materials for advanced lithium batteries. Nat Mater 11:942–947. https://doi.org/10.1038/nmat3435

27. Gao Z, Zhao C, Zhou K et al (2024) Kirkendall effect-induced uniform stress distribution stabilizes nickel-rich layered oxide cathodes. Nat Commun 15:1503. https://doi.org/10.1038/s41467-024-45373-1

28. Li Z, Wang Y, Wang J et al (2024) Gradient-porous-structured Ni-rich layered oxide cathodes with high specific energy and cycle stability for lithium-ion batteries. Nat Commun 15:10216. https://doi.org/10.1038/s41467-024-54637-9

29. Mao Y, Wang X, Xia S et al (2019) High-voltage charging-induced strain, heterogeneity, and micro-cracks in secondary particles of a nickel-rich layered cathode material. Adv Funct Mater 29:1900247. https://doi.org/10.1002/adfm.201900247

30. Asheri A, Rezaei S, Glavas V, Xu BX (2024) Microstructure impact on chemo-mechanical fracture of polycrystalline lithium-ion battery cathode materials. Eng Fract Mech 309:110370. https://doi.org/10.1016/j.engfracmech.2024.110370

31. Singh A, Song J, Li W et al (2024) Microstructure-chemomechanics relations of polycrystalline cathodes in solid-state batteries. Extrem Mech Lett 69:102164. https://doi.org/10.1016/j.eml.2024.102164

32. Chen WX, Allen JM, Rezaei S et al (2024) Cohesive phase-field chemo-mechanical simulations of inter- and trans- granular fractures in polycrystalline NMC cathodes via image-based 3D reconstruction. J Power Sources 596:234054. https://doi.org/10.1016/j.jpowsour.2024.234054

33. Nagda V, Ekström H, Kulachenko A (2024) Impact of mechanical degradation in polycrystalline NMC particle on the electrochemical performance of lithium-ion batteries. J Electrochem Soc 171:060526. https://doi.org/10.1149/1945-7111/ad5622

34. Singh A, Pal S (2022) Chemo-mechanical modeling of inter- and intra-granular fracture in heterogeneous cathode with polycrystalline particles for lithium-ion battery. J Mech Phys Solids 163:104839. https://doi.org/10.1016/J.JMPS.2022.104839

35. Allen JM, Weddle PJ, Verma A et al (2021) Quantifying the influence of charge rate and cathode-particle architectures on degradation of Li-ion cells through 3D continuum-level damage models. J Power Sources 512:230415. https://doi.org/10.1016/j.jpowsour.2021.230415

36. Huang H, Dong S, Lyu Y, Guo ZS (2024) Assessment of inter- and intra-granular fracture behaviors of polycrystalline LiNixCoyMn1-x-yO2 particles during a charging process. Eng Fract Mech 312:110647. https://doi.org/10.1016/J.ENGFRACMECH.2024.110647

37. Paul J, Romeis S, Tomas J, Peukert W (2014) A review of models for single particle compression and their application to silica microspheres. Adv Powder Technol 25:136–153. https://doi.org/10.1016/j.apt.2013.09.009

38. Han J, Sharma N, Zhao K (2024) Computational modeling of coupled mechanical damage and electrochemistry in ternary oxide composite electrodes. J Power Sources 595:234034. https://doi.org/10.1016/j.jpowsour.2023.234034

39. Tang P, Guan S, Wu C et al (2025) Deciphering the crystallographic effect in radially architectured polycrystalline layered cathode materials for lithium-ion batteries. Angew Chem Int Ed. https://doi.org/10.1002/anie.202503108

40. Sadd MH (2020) Elasticity: theory, applications, and numerics. Academic Press, Netherlands

41. Johnson KL (1985) Contact mechanics. Cambridge University Press, Cambridge